Interface properties and microstructural stabilization in elastically inhomogeneous multiphase systems

Danny Perez[1,*] and Laurent J. Lewis[1,†]
[1]*Département de Physique et Regroupement Québécois sur les Matériaux de Pointe (RQMP), Université de Montréal, C.P. 6128, Succursale Centre-Ville, Montréal, Québec, Canada H3C 3J7*
(Received 28 September 2006; published 18 January 2007)

Using a two-dimensional multiscale model based on the classical time-dependent density-functional theory for lattice systems we recently introduced, we numerically study the impact of elastic inhomogeneities on the growth of isolated inclusions in multiphase alloys. We demonstrate that the coupling between the overall interface structure (as determined by the shape of the inclusions) and the local, atomic-scale structure can be very large, and is able to significantly affect the behavior of inclusions during growth. Elasticity is shown to have a strong influence on the local energetics at interfaces, leading to shape modulations and kinetic faceting. Morphological and energetic changes induce oscillations in the chemical potential of the inclusions, opening the way to the stabilization of multi-inclusion microstructures, consistent with experiment. We demonstrate that the interface elastic misfit is a key parameter for controlling the strength of elastic effects.

DOI: 10.1103/PhysRevE.75.011604 PACS number(s): 81.10.−h, 61.66.Dk, 61.72.Qq, 64.75.+g

I. INTRODUCTION

Many properties of materials strongly depend on their atomic-scale and mesoscale structure, such as, e.g., optical absorption and emission [1,2], electrical and thermal conductivity [3], yield strength [4], hardness [5], etc. The design and optimization of high-performance materials thus require their microstructural state to be precisely controlled. However, unlike the chemical composition, the microstructure is difficult to monitor because it results from a delicate competition between many thermodynamical and kinetic processes. Further, it is usually unstable as it continuously evolves through various processes such as diffusion, nucleation, evaporation, etc. Consequently, it is important to understand the energetics of the microstructural state, but also how it evolves in time. The ultimate goal is to gain absolute control over the formation of the microstructure and, once formed, ensure that it is stable in time.

Because they spontaneously form from supersaturated mixtures, multiphase microstructures are ubiquitous in materials science. Discovering strategies for stabilizing them would open the way to important technological applications. As an illustration, it is well known that hardness can be greatly increased by embedding small coherent precipitates (inclusions) within the bulk material [5]. Precipitate hardening occurs because the inclusions are able to pin down dislocations, thereby reducing their mobility. This process, however, is quite sensitive to the size and distribution of the inclusions. The inclusion-matrix interface, for example, usually becomes incoherent for large inclusions, leading to a decrease of the pinning efficiency. The spatial distribution of inclusions must also be such that they can stop most dislocations.

Solid-state multiphase microstructural states are usually not stable because they contain a lot of interfaces. In fact, it was shown by Lifshitz, Slyozov, and Wagner (LSW) [6,7] that if the dynamics results solely from the capillarity-driven reduction of the interfacial free energy, large inclusions tend to grow at the expense of smaller ones—a process called "coarsening"—leading to an increase of the average inclusion size either as $t^{1/3}$ in the diffusion-limited case or $t^{1/2}$ in the attachment-limited case. Ultimately, a microstructure evolving according to the LSW model will consist of a single inclusion. The LSW behavior has been observed in a wide range of multiphase materials in various experimental conditions and geometries, and can therefore be regarded as *normal* coarsening. Returning to the example above, the evolution of the microstructure would lead to a decrease of the hardness of the material resulting from an increase of the size of the inclusions and a concomitant decrease of their number.

Identifying routes to microstructural stabilization in multiphase systems is the purpose of the present study. In order to achieve this goal, it is reasonable to consider systems for which one of the assumptions underlying the LSW theory is violated, viz. (i) the capillarity approximation is valid, i.e., the chemical potential of an inclusion is proportional to the curvature of its interface; (ii) the dynamics is strictly capillarity driven; and (iii) the volume fraction of inclusions is vanishingly small. It is implicit in assumption (ii) that the contribution of the interface to the free energy is large compared to other contributions. It should thus be possible to achieve stabilization by introducing competing terms in the free energy. Since the lattice constants within the inclusions and the matrix are in general different, elastic interactions are an obvious candidate for this purpose. In fact, it is well known that elasticity drastically affects both the morphology and the kinetics of multiphase systems [8]. The effects on morphology range from spontaneous symmetry breaking of the shape of inclusions [9] and the formation of spatial correlations with regards to both shape and position [10–12], to the inversion of the roles of the matrix and the inclusions at high volume fractions [13,14]. Concerning kinetics, the

*Current address: Theoretical Division T-12, Mail Stop B 268, Los Alamos National Laboratory, Los Alamos, NM 87545 USA.
†Author to whom correspondence should be addressed; e-mail: Laurent.Lewis@UMontreal.CA

range of possible behaviors is also large, and both acceleration [12] and (more often) slowdown [11,12,15–20] of the coarsening kinetics have been observed. In fact, complete stabilization has even been reported in some cases. For example, in Ni-Cu-Si alloys [15–17], the evolution initially proceeds normally (i.e., in the manner of LSW), but completely stops (or slows down considerably) once a critical average inclusion size (~10 to 20 nm) is reached; other examples include Ti-Mo [19], Ni-Al-To [12], and Ni-Al-Ti [11] alloys. Further, the slowdown process is accompanied by either an increase [11,12] or a reduction [16] of the width of the distribution of the sizes of the inclusions. In spite of the diversity of behaviors observed, the systems share a common feature: they all possess a large degree of elastic inhomogeneity, i.e., large difference between the elastic constants in the different phases [20]. As a last point, it is also found that coarsening in these materials depends on the volume fraction of the inclusions [16], indicating a violation of assumption (iii). On the other hand, the anisotropy of the elastic constants, while strongly affecting the shape and the distribution of the inclusions, do not appear to influence the coarsening behavior significantly [21,22].

This anomalous behavior—slowdown of the coarsening kinetics—is sometime viewed as a manifestation of inverse coarsening, whereby small inclusions grow at the expense of larger ones. The occurrence of this phenomenon was predicted several years ago [23–25] on the basis of Eshelby's formula for the interaction energy between two spherical inclusions [26]. Eshelby showed that this energy is minimum for soft inclusions if the two have identical sizes. Elastic interactions could thus, in principle, counteract the normal capillarity-driven coarsening process, as suggested above. However, this interpretation suffers from three flaws. First, the formula is only valid for spherical inclusions while it is known that the interaction energy is very sensitive to the shape of the inclusions [27]; numerical simulations where constraints on the shape of the inclusions had been lifted have indeed shown that, while transient inverse coarsening is often observed [28–31], complete stabilization is not expected except when quasiperiodic initial conditions are imposed [28,31]. Second, anomalous coarsening is also observed in systems where the inclusions are harder than the matrix [20], while Eshelby's formula predicts that elasticity should enhance coarsening in this case. Third, inverse coarsening implies a narrowing of the inclusion size distribution, but widening is also observed. Thus, while some observations are consistent with the inverse coarsening theory, the latter evidently cannot account for the whole variety of behaviors observed.

It has recently become possible to carry out large-scale simulations of complex microstructures using phase-field methods. Using such an approach, Onuki and collaborators [13,32] suggested that stabilization was in fact a robust process occurring even in complex microstructures. Their results indicated that coarsening would initially proceed normally, and that a transition to a frozen state would take place suddenly, without the occurrence of inverse coarsening. These conclusions have, however, been questioned by Chen *et al.* who, using a more precise approach for elastic energy calculations [33], did not observe stabilization but, rather, coarsening with a reduced exponent [34]. This exponent was shown to decrease rather slowly, from 0.33 in homogeneous systems to 0.26 for systems with a threefold misfit in shear moduli.

Based on the previous (conflicting) observations, one can conclude that some important physical processes are not properly taken into account in present models. One may speculate that these have to do with the way interfaces are handled, as the studies of coarsening mentioned above implicitly assume that the capillarity approximation (i) is valid. Indeed, the vast majority of models used to study this problem rely on either a sharp-interface [21,28,29,31,35,36] or a phase-field formulation [13,30,32,34,37], where the interphase boundaries are treated as structureless or smooth on the scale of the lattice constant, respectively (exceptions include Refs. [38–41]). In these models, the physical properties of the inclusions are thus continuous functions of shape and size. Since we are concerned with inclusions having radii in the nanometer range and interfaces that are sharp on the nanometer scale [42], the validity of this approximation is not guaranteed. Further, anisotropies in either thermodynamic or kinetic quantities, introduced by the underlying lattice structure, can strongly affect the dynamical behavior of inclusions [43–45]. Finally, it is well known (particularly in the crystal growth community [46]) that the atomic-scale structure of the interfaces can have a dramatic impact on the way solids grow (e.g., continuous vs layer-by-layer), and hence on growth kinetics. For example, coarsening in faceted systems strongly differs from that when the interfaces are rough [47]. An assessment of the validity of assumption (i), and of the consequences of it being violated, could help resolve some of the discrepancies between theory and experiment.

This is what we propose to do in the present article. Following up on previous work where strong interfacial elasticity effects were reported [48], we demonstrate that the interplay between elastic inhomogeneity and atomic-scale interface structure profoundly affects the coarsening behavior of the inclusions. We show that elasticity-induced variations of the attachment energy of solute atoms at different sites at the surface of the inclusions lead to modulations in their shape during growth and, consequently, oscillations in their chemical potential. We show also that the energetics of the sites available for the incorporation of new atoms around the inclusions changes rapidly during growth, increasing the amplitude of the chemical potential variations. Our study establishes that the elastic mismatch at the interface is the primary factor controlling the strength of these effects. We demonstrate, finally, that proper consideration of the atomic structure of the interfaces can account for some of the "peculiar" aspects of coarsening mentioned earlier.

II. MODEL

Since atomic-scale resolution is necessary at interphase boundaries, a simulation method based on a microscopic description of the dynamics is required. To this effect, we recently proposed a multiscale model [49] based on the time-dependent density functional theory (TDDFT) for classical

lattice systems developed by Reinel, Fisher, and collaborators [50–52]. Since a complete description of TDDFT can be found in Ref. [51], and of our particular implementation in Ref. [49] (where we also demonstrate that it can successfully describe elastically inhomogeneous multiphase systems), we only give here, for completeness, a rapid overview of the methodology.

The basic assumption behind TDDFT is that, in typical conditions of microstructural evolution, the only relevant dynamical variables are the site occupation probabilities $p_i^\alpha(t) = \langle n_i^\alpha \rangle_t$—the probability that lattice site i be occupied by a type-α atom at time t—where n_i^α is the number of type-α atoms at site i (either 0 or 1) and $\langle \cdots \rangle_t$ represents the nonequilibrium ensemble average at time t. Implicit in this assumption is that the system can, $\forall t$, be considered to be in local equilibrium relative to the instantaneous values of the p's. A set of reduced equations for the dynamics of the system can then be obtained in terms of the $\{p_i^\alpha(t)\}$ alone. (Other methods based on similar assumptions are described in Refs. [53,54].)

These equations can be derived starting from a microscopic master equation for the probability $P(\mathbf{n},t)$ to find the system in configuration $\mathbf{n}=\{n_i^\alpha\}$ at time t:

$$\frac{dP(\mathbf{n},t)}{dt} = \frac{1}{2} \sum_{i,j \in NN(i)} [w_{i,j}(\tilde{\mathbf{n}})P(\tilde{\mathbf{n}},t) - w_{i,j}(\mathbf{n})P(\mathbf{n},t)]. \quad (1)$$

Here, it is assumed that a configuration evolves in time through successive exchanges of nearest-neighbors particles [$NN(i)$ denotes the set of nearest neighbors of site i]. These exchanges proceed at rate $w_{i,j}(\mathbf{n})$; $\tilde{\mathbf{n}}$ represents a configuration which differs from $\mathbf{n}$ only by the exchange of the occupations of sites i and j.

This equation can be formally written in terms of the $\{p_i^\alpha(t)\}$ as

$$\frac{dp_i^\alpha}{dt} = \sum_{j \in NN(i),\beta} \langle J_{i,j}^{\beta,\alpha} \rangle_t - \langle J_{i,j}^{\alpha,\beta} \rangle_t, \quad (2)$$

with the diffusion fluxes defined as

$$J_{i,j}^{\beta,\alpha}(\mathbf{n}) = n_i^\beta n_j^\alpha w_{i,j}(\mathbf{n}). \quad (3)$$

Equation (2) is the basic equation of TDDFT; the problem is now to compute the nonequilibrium averages. Since a direct calculation of $P(\mathbf{n},t)$ is prohibitive, one must resort to the aforementioned local equilibrium approximation, i.e., $P(\mathbf{n},t) \simeq P^{\text{loc}}(\mathbf{n},t)$ with

$$P^{\text{loc}}(\mathbf{n},t) = \frac{1}{Z(t)} \exp\left\{ -\frac{1}{k_B T}\left[H(\mathbf{n}) + \sum_{i,\alpha} h_i^\alpha n_i^\alpha \right] \right\}, \quad (4)$$

where H is the Hamiltonian of the system, h_i^α is an external site- and species-dependent field, and $Z(t)$ is such that $\Sigma_{\mathbf{n}} P^{\text{loc}}(\mathbf{n},t)=1$. The value of the external field is obtained by requiring self-consistency between $P^{\text{loc}}(\mathbf{n},t)$ and the $\{p_i^\alpha(t)\}$.

Formally, self-consistency is achieved by requiring the grand canonical potential of the system under the external field to be stationary with respect to the average occupations, i.e., the h_i^α are such that

$$\frac{d}{d\mathbf{p}}\Omega(\mathbf{p}) = \frac{d}{d\mathbf{p}}\left[\sum_{i,\alpha} (h_i^\alpha - \mu_{\text{tot}}^\alpha) p_i^\alpha + F(\mathbf{p}) \right] = 0, \quad (5)$$

where $\mathbf{p}=\{p_i^\alpha\}$, μ_{tot}^α is the global chemical potential of species α, and $F(\mathbf{p})$ is the free energy (in terms of the $\{p_i^\alpha\}$). From this last equation, it is now clear that the local fields are proportional to the local chemical potentials

$$h_i^\alpha = \mu_{\text{tot}}^\alpha - \frac{\partial F}{\partial p_i^\alpha} = \mu_{\text{tot}}^\alpha - \mu_i^\alpha. \quad (6)$$

To complete the evaluation of Eq. (2), a free-energy functional $F(\mathbf{p})$ must be specified; we resort to a simple Bragg-Williams mean-field approximation of the form

$$F(\mathbf{p}) = E(\mathbf{p}) - TS(\mathbf{p}) = \frac{1}{2} \sum_{i,j \in NN(i),\alpha,\beta} V_{i,j}^{\alpha,\beta} p_i^\alpha p_j^\beta + k_B T \sum_{i,\alpha} p_i^\alpha \ln p_i^\alpha, \quad (7)$$

with $V_{i,j}^{\alpha,\beta}$ the interaction energy between atom α at site i and atom β at site j. Quantitative agreement with a direct Monte Carlo solution of Eq. (1) cannot be assumed with such a functional, but a qualitatively correct description of the behavior of the different phases is expected.

By also assuming that microscopic configurations change only by vacancy diffusion to a nearest-neighbor site at a rate given by

$$w_{i,j}^\alpha = \nu_0 e^{E_i^\alpha / k_B T}, \quad (8)$$

where E_i^α is the energy of an α-type atom at site i and ν_0 is a trial frequency, a tractable form for Eq. (2) is obtained, namely,

$$\frac{dp_i^\alpha}{dt} = \sum_{j \in NN(i)} M_{i,j}(t)[\mathcal{A}_j^\alpha(t) - \mathcal{A}_i^\alpha(t)], \quad (9)$$

with mobility $M_{i,j}(t) = \langle p_i^{\text{vacancy}}(t) p_j^{\text{vacancy}}(t) \rangle_t \simeq p_i^{\text{vacancy}}(t) p_j^{\text{vacancy}}(t)$ and activity $\mathcal{A}_i^\alpha(t) = e^{-h_i^\alpha(t)/k_B T}$. This equation is a generalized Fick's law where occupation probabilities diffuse from regions of high activity (and hence high chemical potential) to regions of low activity.

The effect of elasticity is introduced through a dependence of the free-energy (7) on the positions of the atoms. At the mean-field level, the free-energy becomes a function of the *average* position of the atom at each lattice site. These positions are obtained by requiring that they minimize the grand potential, i.e.,

$$\frac{d}{d\mathbf{r}}\Omega(\mathbf{p},\mathbf{r}) = \frac{d}{d\mathbf{r}}\left[\sum_{i,\alpha} (h_i^\alpha - \mu_{\text{tot}}^\alpha) p_{\mathbf{l}}^\alpha + F(\mathbf{p},\mathbf{r}) \right] = 0 \quad (10)$$

or, equivalently, that

$$\frac{d}{d\mathbf{r}} E(\mathbf{p},\mathbf{r}) = 0. \quad (11)$$

Here we use a simple harmonic potential to model the elastic interactions between atoms

$$V_{i,j}^{\alpha,\beta} = k^{\alpha,\beta}(r_{i,j} - \sigma^{\alpha,\beta})^2 - \epsilon^{\alpha,\beta}, \quad (12)$$

where $r_{i,j}=|\vec{r}_i-\vec{r}_j|$. As a final point, we note that coherency is assumed at all times, i.e., the neighbors of an atomic site do not change during the course of a simulation; plasticity effects are thus excluded.

Up to now, the formalism has been strictly microscopic, each lattice site being explicitly taken into account. This is clearly not appropriate for the study of large systems consisting of hundreds of thousands or even millions of atoms. However, the variables of interest in the TDDFT calculation—the average occupations and the average positions—vary slowly away from interphase boundaries. Microscopic resolution is thus only needed close to the interfaces, while other regions can be described using fewer degrees of freedom. Exploiting this fact, we proposed a multiscale TDDFT formulation where Eqs. (2) and (11) are solved on nonuniform grids. Taking advantage of the fact that the total occupation probability is conserved, the TDDFT equations can easily be recast into a finite-volume formulation. For flexibility, we choose to work with semistructured grids and adopt the Voronoï volumes of the grid points as volume elements [55,56]. The elastic equilibrium equations are solved (on the same grid) using the quasicontinuum method (QCM) [57]. The QCM relies on a coarse-grainable representation of the displacement field and of the elastic energy to bridge the gap between the microscale and the mesoscale; a recent review of the method and applications can be found in Ref. [58]. In the present study, the QCM is also used in a stand-alone fashion for carrying out elastic energy calculations. In order to use these methods, a representation of the atomic-scale state of the system as a function of the coarse variables must be specified. In our model, this representation is constructed within a "natural-neighbor" framework, namely, Laplace interpolation [55]. This technique also employs the Voronoï tessellation, thus facilitating the management of the grid and the integration with either the finite-volume method or the QCM. Finally, a mechanism to build and update the grid must be specified. In the context of multiphase systems, the distance from the nearest interface provides a very good indication of the appropriate coarseness of the grid, as spatial variations in both occupation probabilities and strain are strongly localized in the neighborhood of interfaces. Atomistic resolution is thus only needed in a narrow region around the latter, while a coarser resolution is adequate farther away into the bulk phase. In our implementation, the local density of grid points is taken to be inversely proportional to the distance to the nearest interface. The details of the grid creation and update procedure can be found in Ref. [49].

III. COMPUTATIONAL DETAILS

A. Simulation setup and parameters

In the calculations reported below, we consider a two-dimensional binary alloy with vacancies (ABv); more precisely, we study the evolution of B-rich inclusions embedded within an A-rich matrix, where the dynamics is governed by the migration of vacancies (i.e., the exchange of atoms with vacancies). The simulation cell is an hexagon with sides of length $1536a_0$ containing about 14 millions sites; the underlying lattice is triangular. Fixed boundary conditions are applied to the elastic equilibrium equations (11) and grand-canonical boundary conditions (fixed chemical potential at the edges of the cell) are applied to Eq. (2). In all cases, the temperature is $T=0.5\epsilon/k_B$, which is about half of the critical temperature for phase separation; the vacancy concentration is taken to be 10^{-3}. All results will be given in dimensionless, reduced units relative to a stress-free pure A phase [see Eq. (12)]: lattice parameter for length (σ) and interaction energy between nearest neighbors for energy (ϵ).

TABLE I. Values of the stiffnesses k_{XY} and lattice constants σ_{XY} for the various types of inclusions considered in the present work. Stiffnesses are in units of ϵ/σ^2 and lattice constants in units of σ.

Type	k_{AA}	k_{AB}	k_{BB}	σ_{AA}	σ_{AB}	σ_{BB}
Homogeneous	0	0	0	1.00	1.00	1.00
HI-LM	50	50	150	1.00	1.03	1.03
HI-HM	50	50	150	1.00	1.00	1.03
SI-LM	50	50	10	1.00	1.00	1.03
SI-LM	50	50	10	1.00	1.03	1.03

Five distinct cases have been studied, each corresponding to a different set of elastic stiffnesses and lattice parameters, as listed in Table I: homogeneous inclusions (no elastic misfit), hard inclusions with low interface misfit (HI-LM), hard inclusions with high interface misfit (HI-HM), soft inclusions with low interface misfit (SI-LM), and finally soft inclusions with high interface misfit (SI-HM). An inclusion is hard (soft) if $k_{BB}>(<)k_{AA}$. The degree of interface misfit qualitatively refers to the difference between σ_{AB} and the typical lattice parameter in the interface region. Since hard inclusions tend to impose their lattice constant to the surrounding matrix, a low interface misfit corresponds to $\sigma_{AB}=\sigma_{BB}$ while a high misfit corresponds to $\sigma_{AB}=\sigma_{AA}$. For soft inclusions, the two situations are inverted. Other parameters of the potential are $\epsilon_{AA}=\epsilon_{BB}=\epsilon$ and $\epsilon_{AB}=0.7\epsilon$. The above choice of parameters will enable us to clearly isolate the effects of "bulk" elasticity (controlled by the values of k_{AA}, k_{BB}, σ_{AA}, and σ_{BB}) from those arising from "interface" elasticity (determined by k_{AB} and σ_{AB}).

B. Method of analysis

In elastically homogeneous systems, the energetics of atoms at interphase boundaries depends only on the nature of neighboring atoms; sites with identical local configurations are therefore equivalent. However, when elastic inhomogeneities are introduced, the problem becomes nonlocal owing to the long range character of elastic interactions. We have recently shown that the nonlocality induces significant changes in the shape, growth mode, and coarsening behavior of inclusions by promoting or impeding the attachment of solute atoms at different sites along the interface [48]. A similar, more exhaustive analysis is reported in the present article; in particular, we demonstrate that a remarkably rich

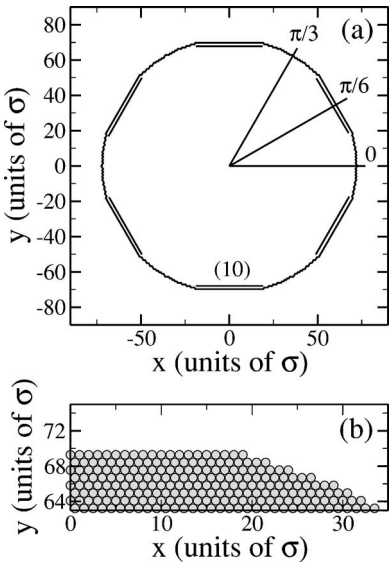

FIG. 1. Model inclusion used in the calculation of substitution elastic energies. (a) General shape of the inclusion; double lines indicate (10) facets; the angular convention used is also shown. (b) Atomic-scale structure of the interface; grey circles correspond to atoms within the inclusion (type B); matrix atoms (type A) are not shown for clarity.

variety of behaviors emerges from the presence of elasticity at interphase boundaries, and that these strongly affect the coarsening process of a collection of inclusions.

Since the growth of inclusions in multiphase systems physically occurs through the substitution of a matrix atom (A) by a solute atom (B) at the interphase boundary, it is essential to understand first how elasticity affects this basic process. The first part of our analysis will thus be concerned with the interplay between the local (atomic scale) and the global (overall shape) elastic effects upon the addition of solute atoms at different sites along the surface of the inclusions; these calculations were carried out within the QCM through sequences of elastic relaxations.

In order to obtain information on the behavior of both faceted and rough regions of the surface, a rounded-hexagonal inclusion with a maximum radius of 70σ was chosen as model system; this is illustrated in Fig. 1(a). Anticipating our results, we note that this configuration is typical of those observed in growth conditions. Due to its symmetric shape, only a small portion of the interface [shown in Fig. 1(b)] needs to be monitored; this contains half the long terrace composing a (10) facet (centered at $\pi/6$), in addition to a rough region containing many small terraces. The elastic addition or substitution energy $\Delta E_{\text{elastic}}^{A\to B}$, i.e., the change in elastic energy resulting from the exchange of an A atom with a B atom at the surface of the inclusion, will be computed for every site along the interface shown in Fig. 1(b). The energies for sequential filling (lateral growth) of terraces on the facet were also computed, in both forward (from the center of the terrace toward the step edge) and backward (from the step edge toward the center of the terrace) directions.

The second part of our analysis will deal with the consequences of elasticity, as determined by the QCM calculations, on the coarsening dynamics of a collection of inclusions; these calculations were performed using the multiscale TDDFT model described in Sec. II. More specifically, we investigate how $\Delta E_{\text{elastic}}^{A\to B}$ affects the shape of the inclusions, their growth, and their chemical potentials. Growth and evaporation were studied using the TDDFT in the grand-canonical ensemble, i.e., with the boundary of the simulation cell acting as constant source or drain of chemical potential. Typically, undersaturations or supersaturations below 0.2% are used in the present study. In all cases, circular inclusions with $R=40\sigma$ were used as the initial configuration. Since the model system studied here is basically a substitutional alloy (notwithstanding the very small vacancy concentration), the inclusions will be characterized by the value of $\Delta\mu_i=\mu_B-\mu_A$, where μ_A and μ_B are the chemical potentials of species A and B inside the (B-rich) inclusions, respectively.

We conclude this section with some remarks on terminology. We frequently refer here to "facets," even if, strictly speaking, these do not exist (in the thermodynamical sense) for 1D interfaces; a more rigorous term would be "quasifacets." In the same spirit, "layer-by-layer" growth strictly occurs only when partial layers behave as a low-dimensional undercritical phase, also rigorously impossible on a 1D interface, even if the filling fraction vs μ curves can be extremely sharp [46]; here we use "layer-by-layer" in a weaker sense to describe growth by successive addition of laterally growing layers.

IV. RESULTS

A. Elastically homogeneous systems

The properties of inclusions (e.g., the interfacial free energy) are affected by the atomic-scale structure along the surface even in absence of elastic misfits. Also, the shape can be modulated by kinetic factors; for example, growth modifies the local curvature of the surface through Mullins-Sekerka shape instabilities [59,60], or its profile through solute trapping [61,62]. These effects usually become significant only for relatively large growth rates. Others, such as kinetic faceting [63,64], can affect slowly moving interfaces; this takes place when faceted orientations grow more slowly than rough orientations, so that fast orientations gradually grow out of existence. This typically occurs at low to moderate growth rates because it requires the chemical potential difference between step sites and terrace sites to be significant compared to the driving force. Conversely, inclusions that suffered evaporation (or dissolution) are more rounded. Since we are mostly concerned with coarsening in the dilute limit here, only low growth rates will be investigated; for larger driving forces, see Ref. [49].

As there is no coupling between the local and the global interface structure in misfit-free systems, the results in this section will serve as a reference for clearly separating elastic effects from other, purely chemical, contributions. Without elastic misfits, elastic substitution energies vanish, and we therefore directly proceed with the TDDFT results.

We investigate first the effect of growth and evaporation. During growth, as can be seen in Fig. 2(a), the shape of the inclusion (initially circular) remains essentially unchanged (cf. continuous line), indicating that thermodynamic or ki-

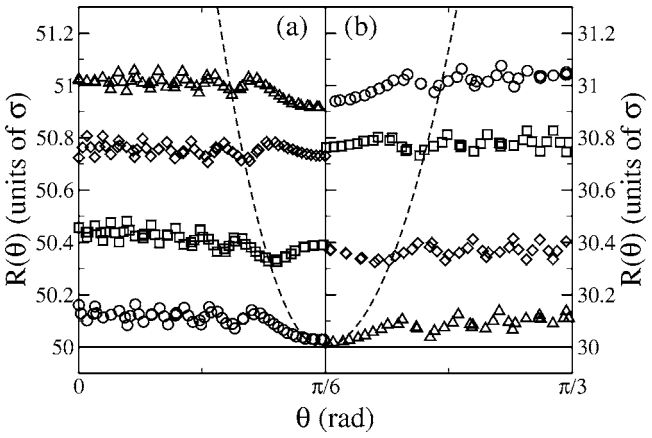

FIG. 2. Angular dependence of the radius $R(\theta)$ of a homogeneous inclusion at different times (a) under growth and (b) under evaporation. θ is defined in Fig. 1; $\pi/6$ corresponds to the center of a (10) facet. Symbols appear in order of increasing time: circles, squares, diamonds, and triangles. The dashed and continuous lines show the expected dependence for a perfect hexagon and a perfect circle, respectively. The initial state of the inclusion is a circle of radius $R=40\sigma$.

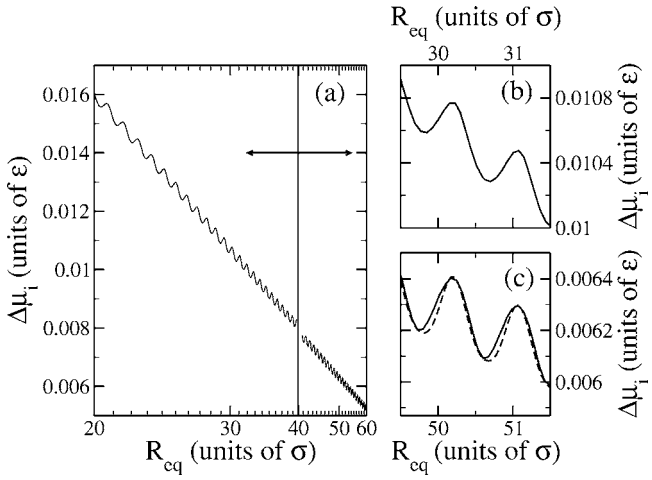

FIG. 3. (a) Chemical potential difference $\Delta\mu_i=\mu_B-\mu_A$ between species B and species A as a function of the size of a homogeneous inclusion during evaporation for $R_{eq}<40\sigma$ (left-pointing arrow) and during growth for $R_{eq}>40\sigma$ (right-pointing arrow). (b) and (c) Close-up views near $R_{eq}=30\sigma$ and $R_{eq}=50\sigma$, respectively.

netic faceting are relatively unimportant at this temperature and for this growth rate. Yet, small modulations in the shape of the inclusion are visible near $\theta=\pi/6$, corresponding to the low-energy (10) plane of the triangular lattice (see Fig. 1). This behavior is the consequence of orientational variations in the interfacial free energy and hence, the concavity of $R(\theta)$ near $\pi/6$ is the signature of a weak faceting tendency in regions of the surface close to (10) orientations. During growth, the inclusion oscillates between this weakly faceted state and a nearly circular one as a function of the filling fraction of the interface layer. A similar behavior is observed for evaporation, Fig. 2(b), supporting the thermodynamic (as opposed to kinetic) origin of the modulations. The importance of this natural tendency to form partially faceted shapes will be demonstrated below. In contrast, away from $\pi/6$ (i.e., in rough regions), $R(\theta)$ increases continuously without deformation as growth proceeds.

Since the chemical potential of an elastically homogeneous inclusion is a function of the curvature of its surface, variations in the latter will affect the former: even a weak tendency to facet changes the average number of A–B bonds per interface atom, and hence the chemical potential of the inclusion. As shown in Fig. 3, oscillations in $\Delta\mu_i$ are indeed observed, superimposed on the usual capillarity $1/R_{eq}$ dependence. The minima correspond to a perfect circular shape while the maxima correspond to a partially faceted shape. As expected, the period of the oscillations [see Figs. 3(b) and 3(c)] is precisely the distance between neighboring (10) atomic layers, that is $\sqrt{3}\sigma/2=0.866\sigma$.

The effect of the shape modulations of an inclusion on $\Delta\mu_i$ can be parametrized using a few simple hypotheses. First, if we assume the inclusion to possess a partially faceted (rounded-hexagonal) shape similar to that shown in Fig. 1, we can write

$$R_{RH}(\theta)=\begin{cases}\dfrac{\sqrt{3}R_0}{\sin(\theta)+\sqrt{3}\cos(\theta)} & \text{if } \left|\theta-\dfrac{\pi}{6}\right|<\theta_f,\\[2ex] \dfrac{\sqrt{3}R_0}{\sin\left(\theta_f+\dfrac{\pi}{6}\right)+\sqrt{3}\cos\left(\theta_f+\dfrac{\pi}{6}\right)} & \text{if } \left|\theta-\dfrac{\pi}{6}\right|>\theta_f.\end{cases} \tag{13}$$

The facets are oriented along the (10) direction and occupy an angular spread $2\theta_f$ ($\theta_f=0$ for a circular inclusion and $\pi/6$ for an hexagonal inclusion). Here, $0<\theta<\pi/3$; values of R_{RH} for θ outside this range are obtained by evaluating the expression at $\theta'=\mathrm{mod}(\theta,\pi/3)$. Second, the chemical potential of a partially faceted inclusion may be written

$$\Delta\mu_i(R_{eq},\theta_f)=\{C+D[\mathrm{exc}(\theta_f)-\mathrm{exc}(0)]\}/R_{eq}+\Delta\mu_i^{\infty}, \tag{14}$$

where C and D are constants related to the interface free-energy, $\mathrm{exc}(\theta_f)$ is such that the excess number of $A-B$ bonds per interface atom for a shape given by Eq. (13) is $\mathrm{exc}(\theta_f)/R_{eq}$ (obtained numerically), and $\Delta\mu_i^{\infty}$ is the value of $\Delta\mu_i$ at thermodynamic coexistence (i.e., between macroscopic phases); C, D, and $\Delta\mu_i^{\infty}$ are treated as adjustable parameters. Third, and finally, we assume that the inclusion oscillates between two states characterized by two angles, θ_f^{max} and θ_f^{min} with a period of $\sqrt{3}\sigma/2$ (see above):

$$\theta_f(R_{eq})=\theta_f^{min}+(\theta_f^{max}-\theta_f^{min})\left[\frac{\sin(4\pi R_{eq}/\sqrt{3}+\phi)+1}{2}\right]. \tag{15}$$

Thus, θ_f^{min} measures the stable departure from the circular shape (for example, in the event of facetting), while $(\theta_f^{max}-\theta_f^{min})$ represents the amplitude of the change in shape in the course of adding (removing) a complete new layer to (from) the inclusion.

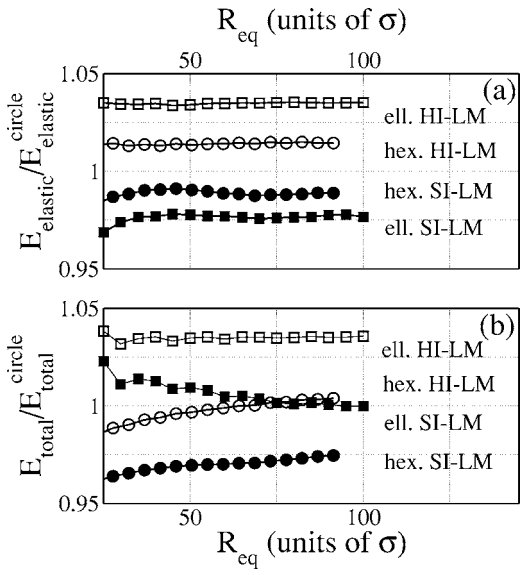

FIG. 4. Energies of various types of inclusions (as indicated) relative to that of a circular inclusion as a function of equivalent radius (i.e., the radius of the circle having identical area): (a) elastic energies; (b) total energies. The elliptic inclusions have an eccentricity of 0.75.

The values of C, D, and $\Delta\mu_\infty$ are obtained by fitting the calculated $\Delta\mu_i$ to Eq. (14), while $\theta_f^{\min}$ $\theta_f^{\max}$ are obtained by fitting to Eq. (13). From the data of Fig. 3, we find $\theta_f^{\min}=0$ and $\theta_f^{\max}=0.07$. Note that these values are valid for all sizes, and for both growth and evaporation. As shown in Fig. 3(c), the agreement between the model and the data is excellent. From now on, the value of D obtained here (5.25) will be kept constant when fitting other $\Delta\mu_i(R_{\rm eq})$ curves to Eq. (14). This will serve as an estimate of the contribution of shape modulations to $\Delta\mu_i$.

Three important consequences can be inferred from the fact that the circular shape is maintained during growth: (i) the interface free-energy is nearly isotropic at the temperature considered; (ii) the kinetic coefficient (related to the growth speed of different orientations of the interface) is isotropic at this temperature and supersaturation; and (iii) shape instabilities are absent for the growth rate considered. Departures from these characteristics will thus be attributed to elasticity.

B. Energetics of inhomogeneous inclusions

Before repeating the previous analysis on misfitted inclusions, we discuss their energetics in order to assess whether interfacially induced shape modifications are favored or impeded by elasticity. These calculations, carried out within the QCM, also provide an estimate of the elastic energies involved.

It is known since Eshelby that, within linear elasticity, hard inclusions have minimum elastic energy when circular and soft inclusions when platelike (very elliptic) [65]. This is verified in our QCM calculations, as shown in Fig. 4(a): The transition to an elliptic shape increases the elastic energy of the HI by about 3% ($\sim 0.07\epsilon$ per B atom), while the elastic energy of the elliptic SI drops by about 2.5% relative to that of the circle ($\sim 0.02\epsilon$ per B atom). In order to assess the cost of faceting, we also considered hexagonal inclusions: the elastic energy increases by 1.5% upon faceting for the HI, while it decreases by roughly the same amount for the SI. Thus, from the energetics point of view, elasticity either promotes (SI) or limits (HI) faceting. However, since the bulk of the excess elastic energy is stored in the tips of the hexagon, partial faceting incurs a relatively low cost in energy. As a final point, it is interesting to note that the relative elastic energies of the different inclusions depend on size, especially at small sizes. This is a manifestation of interface contributions to the elastic energy, which are ignored in conventional linear-elasticity calculations [66].

The spatial distribution of elastic energies is strongly nonuniform. For circular inclusions and harmonic interactions, the energy density is constant inside an inclusion and decays with $1/r^4$ outside, the displacements being proportional to r and $1/r$, respectively [67]. Thus, for hard inclusions—for which most of the deformation occurs within the matrix—the elastic energy is mainly located within a thin region close to the interface [27,30]; in contrast, for soft inclusions, the matrix is only weakly perturbed and the elastic energy is uniformly distributed within the inclusion. This observation emphasizes the importance of a careful treatment the interface region, since the strain varies very rapidly in its vicinity.

Of course, the (chemical) interfacial energy also contributes to determining the equilibrium shape of the inclusions. Using linear elasticity and an interface energy which is isotropic (i.e., does not depend on orientation), Johnson *et al.* [68] have shown that, in two dimensions, the equilibrium shape of the HI is circular for all sizes, while it changes from circular to elliptic (through a second-order transition) with increasing size in the SI. This behavior can also be inferred from our QCM calculations, as demonstrated in Fig. 4(b) which shows the size dependence of the total (elastic plus interfacial) energy. At $T=0$, the interfacial energy is here given by the number of $A-B$ bonds times $\epsilon_{AA}+\epsilon_{BB}-2\epsilon_{AB}=0.3\epsilon$. As can be seen in Fig. 4(b), the elliptic HI is energetically disfavored for all sizes. For the SI, the ellipse initially possesses higher energy than the circle, due to its larger circumference; as size increases, the gain in interfacial energy is eventually offset by the decrease of the elastic energy. This behavior was shown earlier to be correctly described by our TDDFT model [49]. Note that the crossover occurs around $R=100\sigma$; this is above the maximum size considered in the TDDFT calculations (70σ), and we can therefore be confident that the equilibrium shape of all our inclusions is a circle. Finally, owing to the small cost in interfacial energy they incur, faceted inclusions can be energetically advantageous over circular ones. This is the case for both SI and HI, as shown in Fig. 4(b). As the area/perimeter ratio increases, the faceted HI energy eventually increases above that of the circular HI. In contrast, since the elastic energy of the faceted SI is lower than of the circular SI, the former possesses a lower total energy over the whole range of sizes considered here. Of course, this analysis is only valid a $T=0$; as shown in the previous section, finite-temperature entropic contributions offset this energy advantage at $T=0.5\epsilon/k_B$.

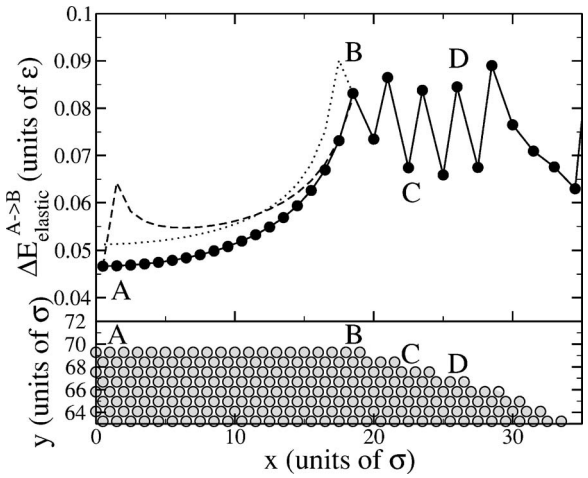

FIG. 5. Change in elastic energy following the substitution of an A atom for a B atom at different positions along the interface of an HI-LM inclusion (filled circles and continuous line); the dashed and dotted lines correspond to forward and backward sequential filling, respectively. Capital letters refer to the various sites along the interface discussed in the text. A: center of the facet; B: edge of the facet; C: step; D: step edge. The bottom panel is the same as Fig. 1(b).

C. Hard inclusions

1. Hard inclusions with low interface misfit (HI-LM)

We undertake now a systematic investigation of the interplay between elasticity, interface structure, and chemical potential in the different types of inclusions, starting with the case of a HI-LM. We begin by examining the elastic contribution to the energy required for substituting a B atom for an A atom at various sites along the surface of the inclusion. The results, presented in Fig. 5, show that $\Delta E^{A\to B}_{\text{elastic}}$ depends sensitively on both the local state of the interface (local atomic configuration) and the overall shape of the inclusion. To illustrate this, consider, for example, the faceted region: while every site along the terrace has the same local neighborhood, $\Delta E^{A\to B}_{\text{elastic}}$ nevertheless varies strongly with position, from 0.045ϵ at the center of the facet (indicated by label A) to 0.085ϵ at the edge (B). We note, in passing, that this is not significantly different from the $\Delta E^{A\to B}_{\text{elastic}}$ for sequential filling of the terrace—which proceeds by substitution at a step instead of directly on the terrace—from either the center or the edge. In the rough region, elasticity slightly favors substitution at steps $[0.065\epsilon$ (C)] over edges $[0.085\epsilon$ (D)], and $\Delta E^{A\to B}_{\text{elastic}}$ is generally larger than on the facet.

This "landscape of addition energies" leads to a slight increase of the stability of terraces on facets in comparison to the misfit-free case. From Fig. 5 we see that the change in elastic energy for evaporating an atom at a step in the rough region is about -0.07ϵ (C), while it ranges between -0.05 and -0.065ϵ at a step on a facet which is sufficiently far from the edge of the terrace (see the curve for forward sequential filling). Terraces on facets therefore tend to be stabilized by elasticity, the more so that they are shorter (since the energy gain in evaporating a B atom is lowest in the middle of the facet).

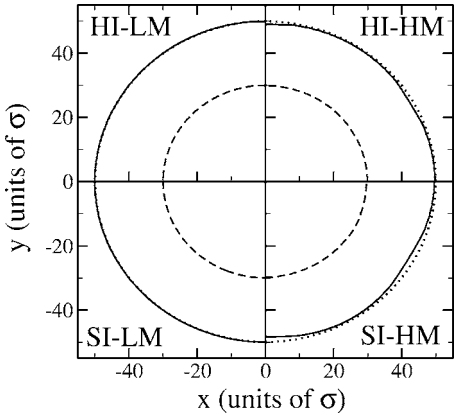

FIG. 6. Shapes of the four types of misfitted inclusions during growth (continuous line) and evaporation (dashed line); the dotted line is a circle of radius $R=50\sigma$ that serves as a reference.

From the point of view of kinetics, the preferential attachment of B atoms at steps (C) vs edges (D) in the rough regions slightly promotes the lateral growth of terraces, leading to the expansion of pre-existing facets. This process is however, self-limiting since the longer the terrace, the larger $\Delta E^{A\to B}_{\text{elastic}}$ at the steps (see the dashed line in Fig. 5). This is related to the increase of elastic energy upon faceting, as reported in Sec. IV B. Thus, we would expect the inclusions to gradually adopt a rounded-hexagonal shape. On the other hand, the low values of $\Delta E^{A\to B}_{\text{elastic}}$ on long terraces have the opposite effect, viz. favoring the nucleation and growth of new terraces (preferably from the center of facets). The inclusion's evolution dynamics will result from a balance between these two competing factors.

Consistent with these observations, the TDDFT simulations reveal that elastic contributions to the shape of the inclusion during growth or evaporation are small; this is clearly seen in Fig. 6 (HI-LM), as well as Fig. 7. Growth and evaporation behave in qualitatively the same way as in the misfit-free case, i.e., continuously, except for small modulations around $\theta=\pi/6$ (Fig. 7). Quantitatively, the shape modulations are slightly more pronounced: fitting to Eq. (13) for $R_{\text{eq}}=50\sigma$ yields $[\theta_f^{\min},\theta_f^{\max}]=[0,0.11]$ here, vs $[0,0.07]$ in the misfit-free case. This is consistent with the discussion above concerning the stabilization of terraces on facets.

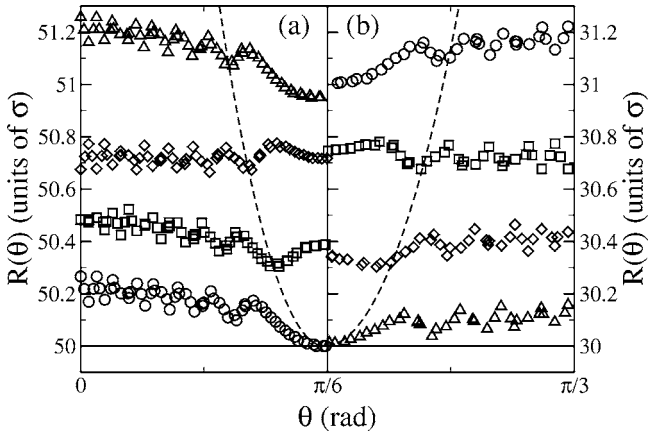

FIG. 7. Same as Fig. 2 for the HI-LM case.

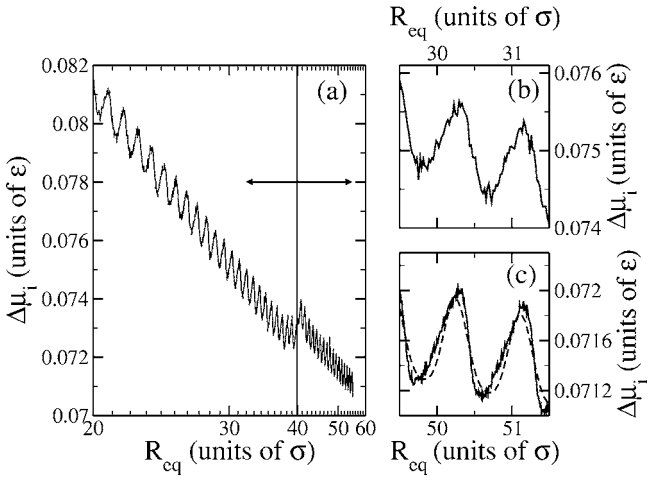

FIG. 8. Same as Fig. 3 for the HL-LM case.

Similar results are obtained in evaporation. Modest kinetic faceting is also observed upon growth, $\theta_f^{\min}$ increasing to 0.03 at $R_{eq}=70\sigma$.

The stabilization of facets can also be inferred from the behavior of the chemical potential of the inclusion, shown in Fig. 8: the amplitude of the oscillations of $\Delta\mu_i$ is here threefold enhanced compared to the homogeneous case. The excellent agreement with the predictions of Eq. (14) [see Fig. 8(c)] confirms that this enhancement is essentially due to the increase of $\theta_f^{\max}$.

2. Hard inclusions with high interface misfit (HI-HM)

We turn now to the HI-HM case; because of the large interface misfit, the effects of elasticity are evidently expected to be more important. The elastic substitution energies, presented in Fig. 9, indeed show an increase in both magnitude and sensitivity to the local and the global interface structure as compared to the HI-LM case.

A first noteworthy feature of the substitution energy landscape is the very large values of $\Delta E_{\text{elastic}}^{A\to B}$ on the facets, which range from 0.125ϵ at the center (A) to 0.18ϵ at the edge (B)—two or three times the barrier for addition at steps in

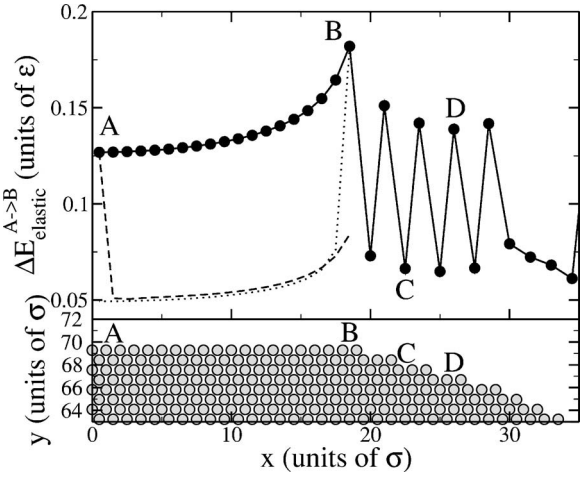

FIG. 9. Same as Fig. 5 for the HI-HM case.

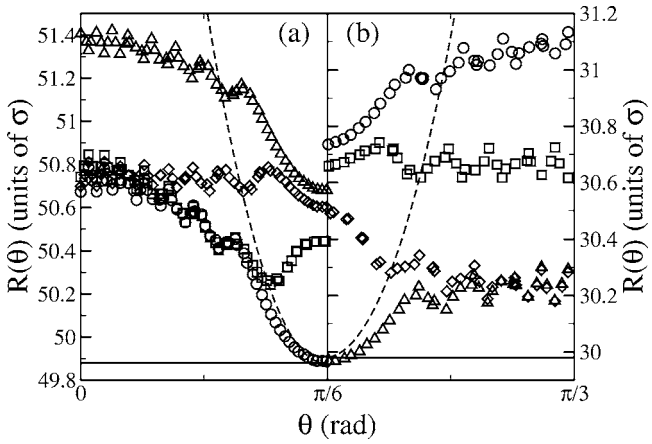

FIG. 10. Same as Fig. 2 for the HI-HM case.

the rough region, 0.065ϵ (C). However, the nucleation of a new terrace on a facet causes $\Delta E_{\text{elastic}}^{A\to B}$ to decrease drastically: the energies for sequentially filling a facet (either from the center or from the edge—see the dashed and dotted lines in Fig. 9) drop to about 0.05ϵ once a first B atom has attached, i.e., *below* the value for steps in rough regions (C). Thus, elasticity imposes a strong barrier to the nucleation of new terraces on facets, but not against their growth once they have started to form. In rough regions, the larger misfit causes an increase of $\Delta E_{\text{elastic}}^{A\to B}$ at step edges to about 0.14ϵ (D), while substitution at steps remains essentially the same as in the low-misfit case $\sim 0.065\epsilon$ (C).

Similar to the HI-LM case, elasticity affects the shape of inclusions by stabilizing terraces on facets: the gain in elastic energy for evaporating an atom is indeed lower from a step on a facet (dotted line) than from a step in the rough region (C). In contrast with the HI-LM case, however, the distribution of $\Delta E_{\text{elastic}}^{A\to B}$ strongly promotes kinetic faceting. Indeed, in addition to the strong bias in favor of the attachment of B atoms at steps in the rough region, which drives the lateral growth of existing terraces, elasticity opposes a large barrier to the nucleation of new terraces on pre-existing facets as noted above, further limiting the growth along these orientations. Thus, rather than competing as in the HI-LM case, these two factors combine now to favor the growth of existing facets. However, as discussed earlier, given the rapid increase of $\Delta E_{\text{elastic}}^{A\to B}$ near the edges of the facets (B), faceting is self-limiting. In addition, the structure of $\Delta E_{\text{elastic}}^{A\to B}$ induces a transition from continuous to lateral layer-by-layer growth on the facets: the nucleation of new terraces preferentially occurs at the center of facets (A) where the substitution energy is smallest; subsequent growth proceeds by sequential filling of the facet, as discussed above.

Enhanced faceting is indeed observed in the TDDFT simulations. Very sharp facets form near $\theta=\pi/6$, as shown in Fig. 10 (cf. circles and dashed line) as well as Fig. 6. Further, the layer-by-layer growth mode anticipated above is also observed: the nucleation of a new layer (squares to diamonds) occurs from the center of an initially clean facet (circles) and is followed by lateral growth (diamonds to triangles). During the first part of the process, the rough region (near $\theta=0$) does not grow appreciably, as it is more advantageous for B atoms

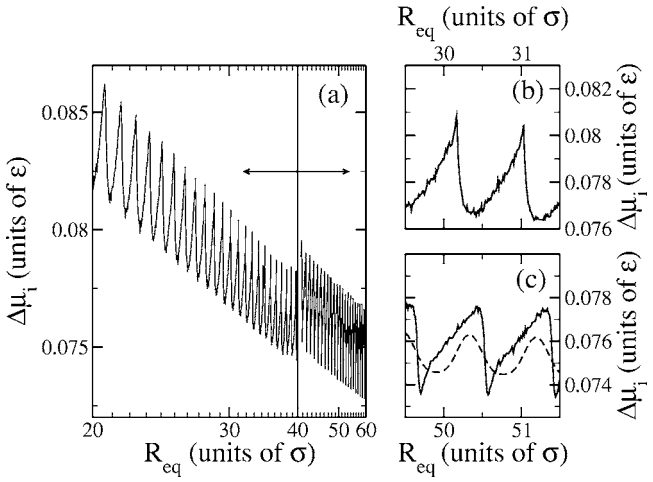

FIG. 11. Same as Fig. 3 for the HI-HM case.

to attach at the steps of the newly formed terrace (near $\theta = \pi/6$). As the latter develops, substitution energies at its steps increases to the point that further growth is gradually outpaced by the growth of rough regions (diamonds to triangles). By then, a complete layer has formed and the cycle repeats itself.

The stabilization of facets also occurs during evaporation. Indeed, the terrace on the facet is the last section of the layer to evaporate; faceting is however less important than during growth. From a fit to Eq. (13), one obtains the following parameters for the facets: $[\theta_f^{\min}, \theta_f^{\max}] = [0.01, 0.15]$, $[0.01, 0.18]$, and $[0.11, 0.18]$ for $R_{\rm eq} \approx 30\sigma$, 50σ, and 70σ, respectively.

The steady increase of $\theta_f^{\min}$ shows that the kinetics strongly contributes to faceting: the high barrier for addition on a clean facet efficiently opposes growth along the corresponding orientation [viz. (10)] compared to that in rough regions. This leads to the development of an increasingly faceted shape.

As shown in Fig. 11, the large modulations in the shape of the inclusion we have just described have a profound effect on the size dependence of $\Delta\mu_i$, which now exhibits very large oscillations during both growth and evaporation. Upon comparing with the predictions of Eq. (14) [cf. Fig. 11(c)], we find however that the oscillations are too large to be accounted for by shape modulations alone. Thus, another process is at play, which can in fact be inferred from the behavior of $\Delta E_{\rm elastic}^{A\to B}$ (Fig. 9) as follows: For partially faceted shapes (corresponding to maxima of $\Delta\mu_i$), low-energy sites are not available for the addition of B atoms because of the high cost of $A \to B$ substitution on top of a facet. Since $\Delta\mu_i$ is the average increase of the free energy for such substitution processes at the interface, high values of $\Delta E_{\rm elastic}^{A\to B}$ translate into high values of $\Delta\mu_i$. However, as soon as the nucleation of a new terrace occurs, low-energy sites become available for other B atoms to attach, causing a drop in $\Delta\mu_i$, in addition to that caused by the shape change. Note that this was not observed in the HI-LM case because $\Delta E_{\rm elastic}^{B\to A}$ does not change significantly following the nucleation of new terraces on facets, and because the substitution energies are much smaller in this case.

It can also be appreciated from Figs. 11(b) and 11(c) that the profile of $\Delta\mu_i$ differs quite a bit from the simple model of Eq. (13). This is a consequence of the peculiar growth behavior of HI-HM: the transition from maxima (clean facets) to minima (nucleation of new terraces on facets) occurs in a very small interval of $R_{\rm eq}$ because the rough regions do not change appreciably during the transition (see Fig. 10), in contrast to either the misfit-free or the HI-LM case. Once the (fast) formation or evaporation of small terraces on facets is completed, the evolution of the rough regions proceeds more uniformly, leading to smoother variations of $\Delta\mu_i$ with $R_{\rm eq}$.

3. Summary of results for hard inclusions

The previous two sections demonstrate that elastic inhomogeneities strongly affect the growth of inclusions. They also highlight the important role played by interfacial elasticity—recall that in both low- and high-misfit cases, the "bulk" elastic properties of inclusions and matrix are the same, while they differ at the interface. At low misfit, the inclusions behave in much the same way as in the homogeneous case. At large misfit, however, the energetics of the addition of solute atoms is significantly modified, with two important consequences: (i) (efficient) kinetic faceting is triggered and gradually pushes the inclusion away from equilibrium; (ii) strong oscillations of the chemical potential develop as a function of the filling fraction of the outer layer (in agreement with our previous results [48]). We stress again here that a proper account of these effects requires an atomic-scale description of the interfaces; this is further warranted by the demonstration of the very strong dependence of the local energetics on both local and global interface structure.

D. Soft inclusions

1. Soft inclusions with low interface misfit (SI-LM)

We now turn to soft inclusions, beginning with the SI-LM case. Given the low misfit, and the low elastic energy stored in soft inclusions, the influence of elasticity on interface properties is expected to be very small. This is in fact confirmed by the elastic substitution energies shown in Fig. 12: $\Delta E_{\rm elastic}^{A\to B} \sim 0.02\epsilon$, compared to $0.05-0.09$ for HI-LM and $0.05-0.18$ for HI-HM. Even more significant is the fact that $\Delta E_{\rm elastic}^{A\to B}$ is almost independent of position along the interface, the variations being $\sim 0.005\epsilon$; we therefore do not expect growth to depend strongly on orientation. In fact, substitution on a facet is totally independent of position, except in the case of sequential filling where $\Delta E_{\rm elastic}^{A\to B}$ decreases abruptly at the edge of the terrace (B). Further, only small energy differences are found between steps and step edges in the rough region. Consequently, the behavior of SI-LM should be quite similar to that of a misfit-free inclusion, except perhaps for a small kinetic faceting tendency arising from the fact that barriers for addition on facets (either on a clean facet or at the steps of a terrace on a facet) are slightly larger than in the rough region.

The TDDFT calculations, presented in Figs. 6 and 13, confirm that the shape of the inclusions during growth and

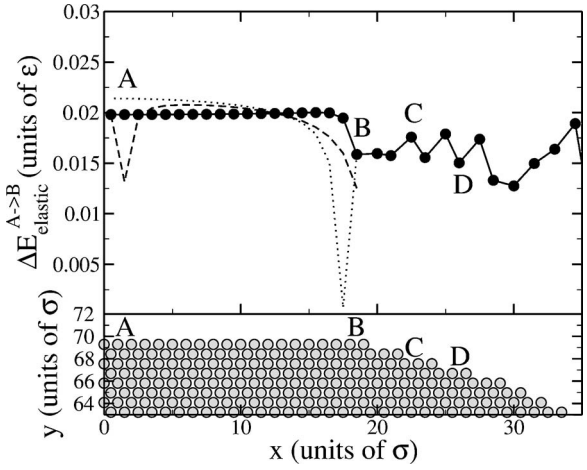

FIG. 12. Same as Fig. 5 for the SI-LM case.

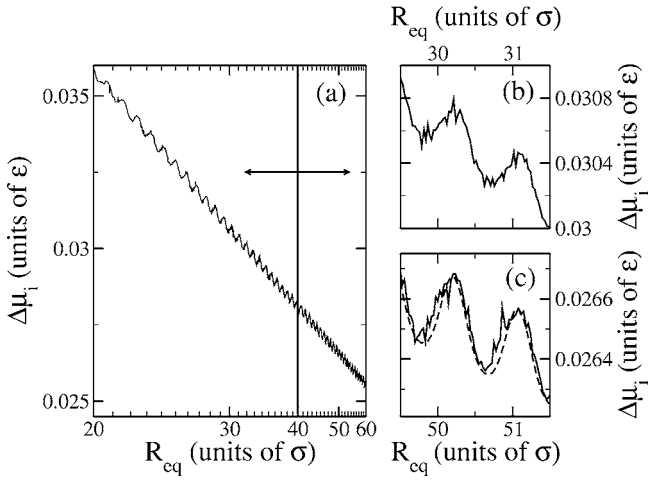

FIG. 14. Same as Fig. 3 for the SI-LM case.

evaporation is essentially unaffected by the small elasticity (compare with Fig. 2). From a fit of $R(\theta)$ to Eq. (13), we obtain $[\theta_f^{\min}, \theta_f^{\max}]=[0, 0.08]$ for both $R_{eq} \sim 30\sigma$ and $R_{eq} \sim 50\sigma$, very close to the misfit-free values ($[0, 0.07]$). Yet, a small kinetic contribution can be detected during growth, as $\theta_f^{\min}$ increases to 0.03 when $R_{eq} \sim 70\sigma$. Note that the inclusion does not spontaneously adopt a faceted shape even if the calculations reported in Sec. IV B indicate that this would lower the total elastic energy. In fact, we observe that the inclusion relaxes to the circular shape even if its initial shape is hexagonal. This shows that entropic effects are strong enough to compensate the energetic advantage of the hexagonal shape at the temperature used.

As shown in Fig. 14, the chemical potential of the inclusion is not significantly affected by the small shape modulations, the latter being nearly identical to that of the misfit-free inclusion. Finally, comparison with Eq. (13) confirms that variations of the chemical potential are essentially caused by shape modulations during growth [see Fig. 14(c)].

2. Soft inclusions with high interface misfit (SI-HM)

We conclude our study of the different types of inclusions with the SI-HM case. The substitution energies are presented in Fig. 15. The misfit is sufficiently large that the elastic energies now depend in a significant manner on the local and global interface structures. In particular, the addition energy clearly decreases as the edge of the terrace (B) is approached. However, sequential filling of the facet from either side strongly modifies this behavior: upon filling from the edge (dotted line in Fig. 15), $\Delta E^{A\to B}_{\text{elastic}}$ jumps from ~ 0 to $\sim 0.02\epsilon$ upon the addition of a single B atom, then slightly increases toward the center of the facet. Likewise, upon filling from the center (dashed line), $\Delta E^{A\to B}_{\text{elastic}}$ forms a little cusp following the addition of the first atom, then gradually decreases toward the edge. Finally, in the rough region, $\Delta E^{A\to B}_{\text{elastic}}$ behaves in much the same way as for hard inclusions: substitution at steps ($\sim 0.02\epsilon$—C) is favored over substitution at step edges ($\sim 0.03\epsilon$—D). Note that the addition energies for sequential filling are slightly larger on facets than in rough regions.

As discussed previously, the behavior of $\Delta E^{A\to B}_{\text{elastic}}$ in the rough region favors the lateral growth of existing terraces. Further, the (slightly) larger values of the addition energies on terraces also favor faceting, as in the HI-HM case. However, unlike hard inclusions, self-limitation of the faceting process is absent; on the contrary, faceting is self-promoting

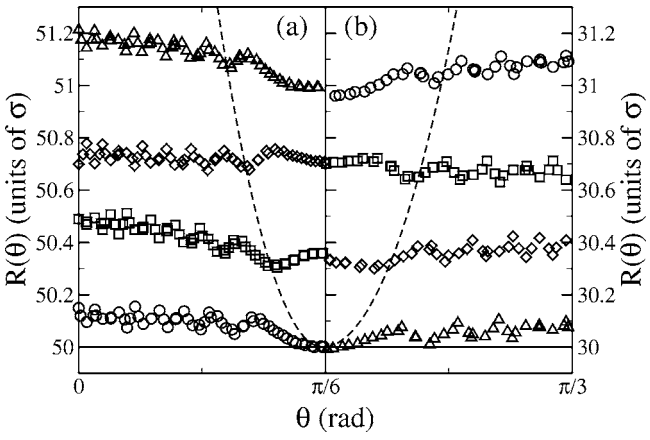

FIG. 13. Same as Fig. 2 for the SI-LM case.

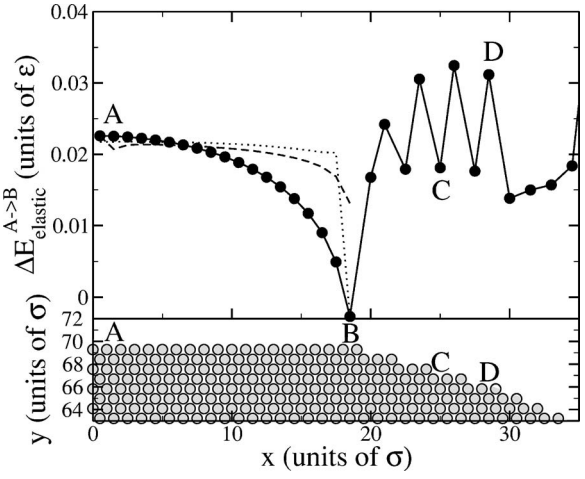

FIG. 15. Same as Fig. 5 for the SI-HM case.

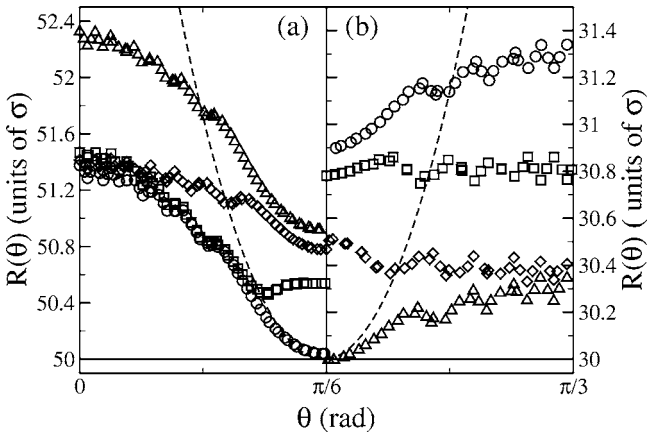

FIG. 16. Same as Fig. 2 for the SI-HM case.

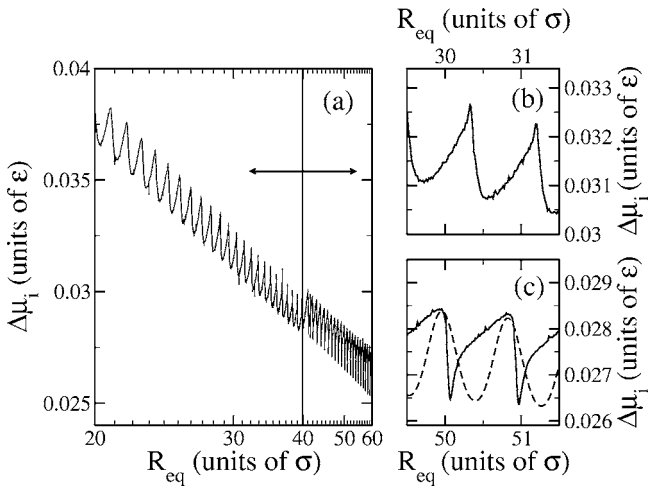

FIG. 17. Same as Fig. 3 for the SI-HM case.

here, as $\Delta E_{\text{elastic}}^{A\to B}$ decreases toward the edge of the facet. This is in agreement with the results of Sec. IV B showing a decrease of the elastic energy upon faceting. Thus, thermodynamics and kinetics concur to promote faceting in the present situation.

TDDFT simulations confirm that faceting is significant in this case, as can be seen in Fig. 6 and, more quantitatively, in Fig. 16: near $\theta=\pi/6$, $R(\theta)$ closely follows the curve corresponding to a perfect facet. Further, deviations from the circular shape are now generalized as $R(\theta)$ remains concave down to $\theta=0$ [recall that $R(\theta)=$cst. for a circular inclusion]. In fact, deviations are so important that $R(\theta)$ can no longer be separated into a facet and a rough region during growth. As in the HI-HM case, the addition of a new layer is initiated from the center of the facets (squares). The new terrace grows by sequential filling (diamonds); once the latter reaches its final size (triangles), addition continues in the rough region. Figure 16 also reveals that evaporation behaves very differently, faceting being now much less important [notice the difference in scale between panels (a) and (b)]. A quantitative analysis of the angular size of the facets during growth gives $[\theta_f^{\min},\theta_f^{\max}]=[0.07,0.21]$ for $R_{\text{eq}}\approx 50\sigma$, reaching $[0.21,0.24]$ for $R_{\text{eq}}\approx 70\sigma$. In contrast, during evaporation, θ_f ranges between 0 and 0.12, providing further evidence for an important kinetic component to faceting.

As in previous cases, oscillations in the shape of the inclusion show up in the behavior of $\Delta\mu_i$, presented in Fig. 17. The impact of kinetic faceting can also be observed in this figure, the amplitude of the oscillations in $\Delta\mu_i$ increasing with size. Comparison with Eq. (14) indicates that these oscillations are essentially due to shape modulations. This result is not surprising given the relatively small values of $\Delta E_{\text{elastic}}^{A\to B}$, and the weaker dependence on the interface state compared to HI-HM.

3. Summary of results for soft inclusions

Given the low elastic energies involved in the relaxation of soft inclusions compared to hard ones, only small deviations from the homogeneous case were expected. This is indeed the situation for low-misfit inclusions, which essentially behave as misfit-free (homogeneous) inclusions. However, upon increasing the interface misfit, strong kinetic faceting develops which induces large oscillations in the chemical potential as a function of increasing size. This once again results from changes in the distribution of elastic substitution energies because of the coupling between local and global interface structure. Note that the magnitude of the elastic substitution energies are quite small here compared to the HI-HM case; still, faceting is much more efficient. This underscores the importance of the self-limitation of kinetic faceting in HI-HM and of self-promotion in SI-LM. These results also demonstrate that small variations in the local energetics of the interface can affect the general behavior during growth, hence the importance of explicitly considering atomic-level elastic contributions.

V. DISCUSSION

Our QCM and TDDFT calculations unambiguously establish the crucial importance of an atomic-scale description of the interface for reproducing the wide variety of possible behaviors induced by interface elasticity. We have shown that the chemical potential is strongly affected by modulations of the shape of the inclusions as well as by the energetics of the interface sites available for incorporating solute *B* atoms. Our calculations also show that chemical potentials which continuously and monotonously decrease with increasing inclusion size are the exception and not the rule as far as inhomogeneous elasticity is concerned. This implies that assumption (i) of the LSW model—the validity of the capillarity approximation, i.e., the chemical potential of an inclusion is proportional to the curvature of its interface—is violated, and hence normal coarsening, $\langle R\rangle\propto t^{1/3}$, does not necessarily take place.

In order to understand the consequences of the chemical potential oscillations on the coarsening behavior of a dilute assembly of inclusions, we have constructed and numerically solved a generalized LSW model which, as with the original LSW model [6], provides an equation of motion for the evolution of the size distribution $f(t,R)$ of the assembly:

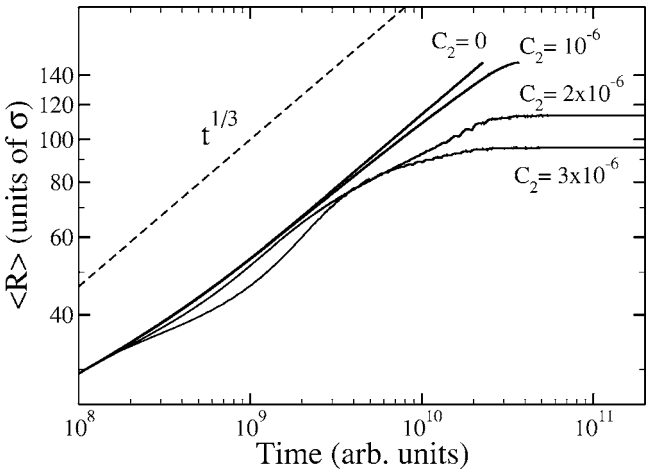

FIG. 18. Average inclusion size for different values of the parameter C_2 as obtained using the modified LSW model (see text for details).

$$\frac{\partial f(t,R)}{\partial t} = -\frac{\partial}{\partial R}\left[\frac{dR}{dt} f(t,R)\right], \tag{16}$$

where dR/dt is the rate at which an inclusion of radius R grows. By analogy with Eq. (9), one gets

$$\frac{dR}{dt} \propto \frac{1}{R}[\mathcal{A}_m - \mathcal{A}_I(R)], \tag{17}$$

where $\mathcal{A}_m$ and $\mathcal{A}_I(R)$ are the activities within the matrix and inclusion, respectively; for simplicity, the vacancies are ignored. The activity of the matrix is taken to be proportional to the solute supersaturation $\Delta(t)$, while the activity of the inclusion follows a modified Gibbs-Thomson behavior

$$\mathcal{A}_m(t) = \Delta(t), \tag{18}$$

$$\mathcal{A}_i(t) = C_1/R + C_2[\cos(4\pi R/\sqrt{3}) + 1]/2 \tag{19}$$

with C_1 and C_2 arbitrary constants; note that setting $C_2=0$ recovers the original LSW model. In order to close the system of equations, we must enforce conservation of solute atoms

$$Q_0 = \Delta(t) + \int_0^\infty \pi R^2 f(R,t) dR, \tag{20}$$

where Q_0 is the initial, total supersaturation.

In what follows, we set $C_1=0.00025\sigma^{-1}$ and vary the value of C_2 between 0 and 3×10^{-6}; $f(0,R)$ is (arbitrarily) taken to be constant between $R=13\sigma$ and 21σ and zero elsewhere. The average inclusion size [obtained by numerically integrating Eq. (16)] is presented in Fig. 18. This figure shows that the chemical potential oscillations [or equivalently, the activity oscillations, Eq. (19)] do not affect the early stages of coarsening, which exhibits the normal LSW behavior (dashed line). However, when the amplitude of the oscillations (as determined by C_2) gets sufficiently large, coarsening is completely inhibited in later stages: after a transient period where the growth exponent gradually decreases, the system becomes kinetically frozen and the size

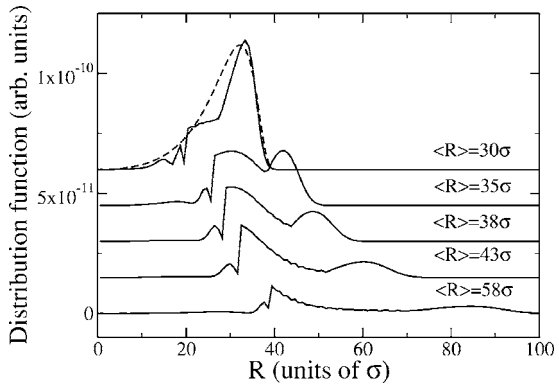

FIG. 19. Size distribution function $f(t,R)$ at various average size (and thus time) for $C_1=0.00025\sigma^{-1}$ and $C_2=3\times10^{-6}$. The dashed line is the LSW result ($C_2=0$); the different curves have been shifted for clarity.

distribution function ceases to evolve. The stabilization of the average inclusion size is not caused by some sort of inverse coarsening, which would imply gradual narrowing of the size distribution. In fact, the opposite is true: the distribution widens with time, as shown in Fig. 19 for $C_2=3\times10^{-6}$. For $\langle R\rangle \leq 30\sigma$, the size distribution is little affected by the oscillations in the chemical potential, as it is close to the predictions of the classical LSW model (dashed line). However, as time runs (and $\langle R\rangle$ gets larger), the small R section of $f(R,t)$ rapidly becomes frozen, while the large R maximum moves toward larger values, causing the formation of a gradually widening bimodal distribution. The large size peak gradually decays, leaving a long tail in its wake, until coarsening completely stops.

This behavior can be understood in terms of the growth rate of the inclusions dR/dt, Eq. (17); the results for this quantity are presented in Fig. 20. The main consequences of the oscillations is that dR/dt possesses multiple zeroes, in contrast to the pure-capillarity case which has only one zero at any given time. This difference is of great significance because it implies that a finite fraction of the inclusions can simultaneously be in equilibrium at the same supersaturation, while this fraction is vanishingly small for smooth chemical potentials. For small average size $\langle R\rangle$ (see $\langle R\rangle=30\sigma$ in Fig.

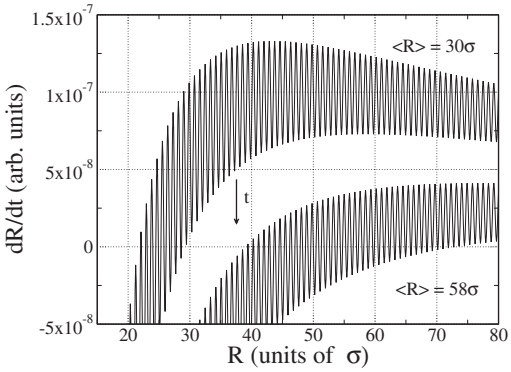

FIG. 20. Growth rate dR/dt [Eq. (17)] at two values of the average size for $C_1=0.00025\sigma^{-1}$ and $C_2=3\times10^{-6}$; the increase in the average size is a measure of time since the system is in a coarsening mode.

20), equilibrium ($dR/dt=0$) is only possible over a rather small range of sizes (roughly between $R=22\sigma$ and $R=28\sigma$), so that the effect on the overall dynamics of the system is limited and coarsening proceeds normally. For larger average inclusion size (see $\langle R\rangle=58\sigma$ in Fig. 20), the range of possible equilibrium states expands (to $R=40\sigma-75\sigma$), causing a gradual freezing of the distribution function. In fact, only the two extremes of the distribution (in regions where the growth rate does not cross the equilibrium $dR/dt=0$ line) are able to evolve, causing the formation of a bimodal distribution and, subsequently, of a large size tail. Eventually, the whole distribution function is located in regions where equilibrium with the matrix is possible, causing the coarsening to completely stop.

These results demonstrate, again, that the oscillations of the chemical potential during growth significantly affect the coarsening behavior of the inclusions, and can even lead to a complete stabilization of the microstructure without appealing to inverse coarsening. Indeed, a rapid decrease of the coarsening exponent from 1/3 at early times to 0 at later times is observed. The oscillations can also strongly modify the size distribution of the inclusions through the formation of a large size tail.

The $\langle R\rangle$ vs t curves presented in Fig. 18 are in striking agreement with the behavior observed in such elastically inhomogeneous alloys as Ni-Cu-Si and Ti-Mo [20]. In these systems, coarsening initially proceeds according to the LSW theory with a growth exponent of 1/3, then abruptly stops. We note that, in contrast to this, recent large-scale phase-field simulations have predicted that coarsening proceeds with a reduced, but constant, exponent in elastically inhomogeneous systems [34]. In view of the agreement of our findings with experiment, we may conclude that the physical process responsible for microstructural stabilization in elastically inhomogeneous alloys is not properly included in phase-field models; our calculations indicate that the "missing link" is interface, atomic-scale elasticity. In addition, the oscillations in the chemical potential very likely explain the widening of the size distribution function observed during slow coarsening in some alloys [11,12,69], as discussed above.

It must nevertheless be mentioned that the present analysis suffers from two limitations. First, coarsening is assumed to arise strictly from the thermodynamic driving force $\mathcal{A}_m - \mathcal{A}_I(R)$. In real materials, thermal fluctuations enhance coarsening by helping the system to escape from long-lived metastable states even if the thermodynamic driving force alone is insufficient for this. For example, the nucleation of new terraces onto a facet of an HI-HM would abruptly decrease the chemical potential of an inclusion, allowing it to grow further. What was identified as a transition from a coarsening state to a frozen state in the present model is in fact a transition from diffusion-limited coarsening to nucleation-limited coarsening. For small nucleation barriers, thermal fluctuations enable coarsening to continue, albeit at a very small rate, while as shown by Rohrer and collaborators [70], higher barriers (compared to k_BT) virtually stop coarsening on experimental timescales. Second, it is known from experiment that the volume fraction of the inclusions affects coarsening in elastically inhomogeneous systems [18,20]; this is not taken into account here. Thus, the slowdown of the kinetics is most likely not the result of interface effects alone. The impact of direct interactions between inclusions through the long-ranged strain field will be the subject of future investigations.

An aspect that has not been considered here it that metallic alloys are generally elastically anisotropic, implying the presence of "soft" orientations along which inclusions have a tendency to align. Consequently, inclusions usually adopt a cuboid shape with well-defined facets. Interface elasticity could thus be even more important in elastically anisotropic systems since, with large facets, the spectrum of addition energies is likely to become very wide, leading to larger oscillations of the chemical potential and hence larger impact on coarsening.

VI. CONCLUSION

We have studied the role of interfacial elastic effects on the behavior of inhomogeneous inclusions under growth or evaporation conditions using a two-dimensional model based on the classical TDDFT formalism. This was achieved by decoupling the effect of "bulk" misfit from the effect of "interface" misfit through independent variations of the intraspecie and interspecie terms of the interatomic potential. While it is already well known that strong inhomogeneities are able to considerably modify the coarsening behavior of the inclusions, our results show that the level of interface misfit is also crucially important: at low interface misfit, the behavior of isolated inclusions is similar to that of elastically homogeneous inclusions but a high interface misfit induces very strong coupling between the global shape of the inclusions and its structure on a local, atomic scale. This alters the energetics of the interface by favoring incorporation of solute atoms at certain specific sites. In turn, the new energy landscape modifies the morphology of the inclusions during growth, and hence the chemical potential of the inclusions. Oscillations of the chemical potential following the addition or subtraction of a new layer around the inclusion are shown to be commonplace in elastically inhomogeneous systems at high interface misfit. Using a modified LSW model, we have shown that, in presence of these oscillations, coarsening initially proceeds normally (with a 1/3 exponent) but eventually stops completely, leading to stabilization of the microstructure. The results are in good qualitative agreement with the experimental studies of some inhomogeneous alloys [18,20]. These results stress the need for an atomistic treatment of the interfaces in elastically inhomogeneous systems in order to unravel the wide range of possible growth behaviors, each having distinct kinetic properties.

ACKNOWLEDGMENTS

This work has been supported by grants from the Natural Sciences and Engineering Research Council of Canada (NSERC) and the *Fonds Québécois de la Recherche sur la Nature et les Technologies* (FQRNT). We are indebted to the *Réseau Québécois de Calcul de Haute Performance* (RQCHP) for generous allocations of computer resources.

[1] J. C. M. Garnett, Philos. Trans. R. Soc. London, Ser. A **203**, 385 (1904).
[2] S. Schmitt-Rink, D. S. Chemla, and D. A. B. Miller, Adv. Phys. **38**, 89 (1988).
[3] S. Torquato, S. Hyun, and A. Donev, Phys. Rev. Lett. **89**, 266601 (2002).
[4] A. C. Reddy and S. S. Rajan, Bull. Mater. Sci. **28**, 75 (2005).
[5] P. D. Merica, Trans. Am. Inst. Min., Metall. Pet. Eng. **99**, 13 (1932).
[6] I. M. Lifshitz and V. V. Slyozov, J. Phys. Chem. Solids **19** 35 (1961).
[7] C. Wagner, Z. Elektrochem. **65**, 581 (1961).
[8] P. Fratzl, O. Penrose, and J. L. Lebowitz, J. Stat. Phys. **95**, 1429 (1999).
[9] A. Maheshwari and A. J. Ardell, Phys. Rev. Lett. **70**, 2305 (1993).
[10] Y. S. Yoo, D. Y. Yoon, and M. F. Henry, Met. Mater. (Soeul, Rep. Korea) **1**, 47 (1995).
[11] A. Ges, O. Fornaro, and H. Palacio, J. Mater. Sci. **32**, 3687 (1997).
[12] H. A. Calderon, G. Kostorz, Y. Y. Qu, H. J. Dorantes, J. J. Cruz, and J. G. Cabanas-Moreno, Mater. Sci. Eng., A **238**, 13 (1997).
[13] A. Onuki and H. Nishimori, Phys. Rev. B **43**, 13649 (1991).
[14] P. H. Leo, J. S. Lowengrub, and H. J. Jou, Acta Mater. **46**, 2113 (1997).
[15] S. Yoshida, M. Fukaya, and T. Miyazaki, J. Jpn. Inst. Met. **51**, 18 (1987).
[16] T. Miyazaki and M. Doi, Mater. Sci. Eng., A **110**, 175 (1989).
[17] M. Doi, T. Miyazaki, and T. Wakatsuki, Mater. Sci. Eng. **67**, 247 (1984).
[18] T. Miyazaki, in *Solid-Solid Phase Transformations*, edited by D. L. W. C. Johnson, J. M. Howe, and W. Soffa (The Minerals, Metals and Materials Society, Warrendale, PA, 1994).
[19] F. Langmayr, P. Fratzl, G.Vogl, and W. Miekeley, Phys. Rev. B **49**, 11759 (1994).
[20] O. Paris, F. Langmayr, G. Vogl, and P. Fratzl, Z. Metallkd. **86**, 860 (1995).
[21] K. Thornton, N. Akaiwa, and P. W. Voorhees, Phys. Rev. Lett. **86**, 1259 (2001).
[22] K. Thornton, N. Akaiwa, and P. W. Voorhees, Acta Mater. **52**, 1365 (2004).
[23] Y. Enomoto and K. Kawasaki, Acta Metall. **37**, 1399 (1989).
[24] W. C. Johnson, T. A. Abinandanan, and P. W. Voorhees, Acta Metall. Mater. **38**, 1349 (1990).
[25] T. A. Abinandanan and W. C. Johnson, Acta Metall. Mater. **41**, 27 (1992).
[26] J. D. Eshelby, Acta Metall. **14**, 1306 (1966).
[27] A. Onuki and H. Nishimori, J. Phys. Soc. Jpn. **60**, 1 (1991).
[28] C. H. Su and P. W. Voorhees, Acta Mater. **44**, 1987 (1996).
[29] H. J. Jou, P. H. Leo, and J. S. Lowengrub, J. Comput. Phys. **131**, 109 (1997).
[30] D. Orlikowski, C. Sagui, A. Somoza, and C. Roland, Phys. Rev. B **59**, 8646 (1999).
[31] I. Schmidt, Comput. Mater. Sci. **22**, 333 (2001).
[32] A. Onuki and A. Furukawa, Phys. Rev. Lett. **86**, 452 (2001).
[33] S. Hu and L. Q. Chen, Acta Mater. **49**, 1879 (2001).
[34] J. Zhu, L. Q. Chen, and J. Shen, Modell. Simul. Mater. Sci. Eng. **9**, 499 (2001).
[35] K. Thornton, N. Akaiwa, and P. W. Voorhees, Acta Mater. **52**, 1353 (2004).
[36] X. Li, K. Thornton, Q. Nie, P. W. Voorhees, and J. S. Lowengrub, Acta Mater. **52**, 5829 (2004).
[37] L. Q. Chen, Annu. Rev. Mater. Sci. **32**, 113 (2002).
[38] J. K. Lee, Scr. Metall. Mater. **32**, 564 (1994).
[39] P. Fratzl and O. Penrose, Acta Metall. Mater. **43**, 2921 (1995).
[40] J. M. Liu, Mater. Lett. **28**, 189 (1996).
[41] H. Gupta, R. Winkamer, P. Fratzl, and J. L. Lebowitz, Acta Mater. **49**, 53 (2001).
[42] K. Thornton, J. Agren, and P. W. Voorhees, Acta Mater. **51**, 5675 (2003).
[43] L. N. Brush and R. F. Sekerka, J. Cryst. Growth **96**, 419 (1989).
[44] E. Yokoyama and R. F. Sekerka, J. Cryst. Growth **125**, 389 (1992).
[45] T. Uehara and R. F. Sekerka, J. Cryst. Growth **254**, 251 (2003).
[46] B. Mutaftschiev, *The Atomistic Nature of Crystal Growth*, Springer Series in Materials Science (Springer, Berlin, 2001).
[47] G. S. Rohrer, C. L. Rohrer, and W. W. Mullins, J. Am. Ceram. Soc. **84**, 2099 (2001).
[48] D. Perez and L. J. Lewis, Phys. Rev. Lett. (to be published).
[49] D. Perez and L. J. Lewis, Phys. Rev. E **74**, 031609 (2006).
[50] D. Reinel and W. Dieterich, J. Chem. Phys. **104**, 5234 (1996).
[51] H. P. Fischer, J. Reinhard, W. Dieterich, J. F. Gouyet, P. Maass, A. Majhofer, and D. Reinel, J. Chem. Phys. **108**, 3028 (1998).
[52] M. Kessler, W. Dieterich, H. L. Frisch, J. F. Gouyet, and P. Maass, Phys. Rev. E **65**, 066112 (2002).
[53] M. Plapp and J. F. Gouyet, Phys. Rev. E **55**, 5321 (1997).
[54] L. Q. Chen, Phys. Rev. B **58**, 5266 (1998).
[55] N. Sukumar, Int. J. Numer. Methods Eng. **57**, 1 (2003).
[56] R. Eymard, T. Gallouët, and R. Herbin, IMA J. Numer. Anal. **26**, 326 (2006).
[57] E. B. Tadmor, R. Phillips, and M. Ortiz, Langmuir **12**, 4529 (1996).
[58] R. E. Miller and E. B. Tadmor, J. Comput.-Aided Mater. Des. **9**, 203 (2002).
[59] W. W. Mullins and R. F. Sekerka, J. Appl. Phys. **34**, 323 (1963).
[60] P. H. Leo and R. F. Sekerka, Acta Metall. **37**, 3139 (1989).
[61] M. Hillert, Acta Mater. **47**, 4481 (1999).
[62] J. S. Langer and R. F. Sekerka, Acta Metall. **23**, 1225 (1975).
[63] G. Wulff, Z. Kristallogr. **34**, 449 (1901).
[64] F. C. Frank, *Growth and Perfection of Crystals* (John Wiley, New York, 1958), Chap. On the kinematic theory of crystal growth and dissolution processes, p. 411.
[65] J. D. Eshelby, Proc. R. Soc. London, Ser. A **241**, 376 (1957).
[66] P. Sharma and S. Ganti, J. Appl. Mech. **71**, 663 (2004).
[67] T. Mura, Micromechanics of Defects in Solids, 2nd ed. (Kluwer Academic, Dordrecht, 1987).
[68] W. C. Johnson and J. W. Cahn, Acta Metall. **32**, 1925 (1984).
[69] H. J. Ryu, S. H. Hong, J. Weber, and J. H. Tundermann, J. Mater. Sci. **34**, 329 (1999).
[70] G. S. Rohrer, C. L. Rohrer, and W. W. Mullins, J. Am. Ceram. Soc. **85**, 675 (2002).